



# Preparation of $\text{La}_{1-x}\text{Ca}_x\text{MnO}_3$ perovskite–graphene composites as oxygen reduction reaction electrocatalyst in alkaline medium

Jie Hu <sup>a, b</sup>, Lina Wang <sup>a</sup>, Lina Shi <sup>a</sup>, Hao Huang <sup>b, \*</sup>

<sup>a</sup> Hebei Key Laboratory of Applied Chemistry, Department of Environment and Chemistry, Yanshan University, Qinhuangdao 066004, PR China

<sup>b</sup> State Key Laboratory of Metastable Materials Science & Technology, Yanshan University, Qinhuangdao 066004, PR China

## HIGHLIGHTS

- $\text{La}_{1-x}\text{Ca}_x\text{MnO}_3$ –graphene composites were synthesized for the first time.
- Oxygen reduction reaction activity of composites in alkaline medium was evaluated.
- The electrocatalytic activity of composites was enhanced than pure  $\text{LaMnO}_3$  oxides.
- Doping Ca enhance the electrochemical performance of  $\text{LaMnO}_3$ –graphene composites.

## ARTICLE INFO

### Article history:

Received 10 April 2014

Received in revised form

25 June 2014

Accepted 1 July 2014

Available online 9 July 2014

### Keywords:

Perovskite

Graphene

Alkaline electrolyte

Oxygen reduction reaction

Electrocatalyst

## ABSTRACT

$\text{La}_{1-x}\text{Ca}_x\text{MnO}_3$  perovskite–graphene composites are synthesized as catalysts for Zn–air cell cathodes. The samples are characterized by thermogravimetry–differential thermal analysis, X-ray diffraction, scanning electron microscopy, transmission electron microscopy, and X-ray photoelectron spectroscopy. Results show that perovskite particles are homogeneously dispersed on graphene nanosheets, and that doping Ca does not change the perovskite structure. Electrochemical properties are investigated by galvanostatic discharge, linear sweep voltammetry, and electrochemical impedance spectroscopy techniques.  $\text{LaMnO}_3$ –graphene composites show superior performance than pure  $\text{LaMnO}_3$ . Doping Ca into the composites can tune their catalytic activity and sample prepared with  $x = 0.4$  possesses the highest electrocatalytic activity. The measurement of the rotating ring-disk electrode reveals that the electron transfer number of  $\text{La}_{0.6}\text{Ca}_{0.4}\text{MnO}_3$ –graphene is 3.6. These results indicate that the  $\text{La}_{1-x}\text{Ca}_x\text{MnO}_3$ –graphene composites are potential air electrodes catalysts.

© 2014 Elsevier B.V. All rights reserved.

## 1. Introduction

Zinc–air fuel cells (ZAFCS) are a potential energy generator because of their high specific energy, with a theoretical energy of  $1350 \text{ W h kg}^{-1}$  and theoretical cell voltage of  $1.65 \text{ V}$  [1]. This characteristic leads to low-cost fuels of metallic zinc and air and environmentally friendly byproducts. ZAFCS has attracted considerable attention because it can use inexpensive metal oxides as catalysts and does not cause problems in compression and storage of explosive or flammable fuels [2]. Oxygen reduction reaction (ORR) mainly occurs at the air cathode, the efficiency of this reaction is important to the cell. The noble metal Pt has been widely investigated for its electrocatalytic performance during ORR reactions in alkaline electrolytes [3–8]. However, the high cost of Pt limited its use. Therefore, current research on ORR catalysts in

alkaline electrolytes had been focused on enhancing the catalytic activities, decreasing the amounts of precious metals, and developing low-cost metal based catalyst materials. [9–12]. Perovskite are promising catalysts for metal–air batteries because of their high catalytic activity and low-cost. A feature of perovskite that is attractive to researchers is the ability to incorporate a wide variety of cations (differing species and doping levels) that allows for a wide range of doping possibilities [13]. Studies reported that La-based perovskite exhibit promising ORR activities in alkaline electrolytes [14–16]. However,  $\text{LaMnO}_3$  have insufficient electrochemical stability in ORR process, because an additional phase of the lanthanum hydroxide is in the composition of their structure. The additional phase causes the instability of lanthanum [17]. Therefore, a carbon support is necessary as an electron conducting path for a practical use of  $\text{LaMnO}_3$  as an electrocatalyst.

Graphene is a single layer of  $\text{sp}^2$ -bonded carbon atoms. It has received considerable attention because of its high conductivity and high surface area. Electrical performance can lead to the

\* Corresponding author. Tel.: +86 15369700375.

E-mail addresses: [huanghao@ysu.edu.cn](mailto:huanghao@ysu.edu.cn), [huanghao1977@163.com](mailto:huanghao1977@163.com) (H. Huang).

application of graphene in the next generation of electronic components and energy-storage materials, such as capacitors and batteries, transparent conducting electrodes, and mechanical resonators [18]. Increasing studies [19–22] have reported on nitrogen-doped graphene and graphene-supported noble metal catalyst (Pt, Pd, Ag and Au) for highly active oxygen reduction reaction in alkaline condition. Recently, there are a few attempts to combine oxides with graphene as electrocatalysts for ORR in alkaline electrolytes. For instance, Liang et al. reported a hybrid material consisting of  $\text{Co}_3\text{O}_4$  nanocrystals grown on reduced graphene oxide as a high-performance catalyst for the oxygen reduction reaction [23]. Then, they reported that covalent hybrid of spinel manganese–cobalt oxide and graphene as advanced oxygen reduction electrocatalysts, which increased the activity of the catalytic sites in the hybrid materials, further boosting the ORR activity compared to the pure cobalt oxide hybrid [24]. Wu et al. reported a kind of 3D nitrogen-doped graphene aerogel-supported  $\text{Fe}_3\text{O}_4$  nanoparticles as efficient electrocatalysts for the ORR [25]. Results show that these composites exhibit good oxygen reduction activity. Therefore,  $\text{LaMnO}_3$  modified by graphene may be an effective approach to increase its catalytic activity and stability for the ORR.

To date, some investigations have focused on  $\text{LaMnO}_3$ –graphene composites photocatalyst [26] and obtained good results. Studies on combination of  $\text{LaMnO}_3$  and graphene for alkaline fuel cells and metal–air batteries are not been reported. In this paper,  $\text{LaMnO}_3$  was modified by graphene as catalyst of ZAFC cathode, and the grains of  $\text{LaMnO}_3$  were homogeneously spread on the graphene nanosheets. The electrocatalytic activity of composites was enhanced compared to pure  $\text{LaMnO}_3$  because of its special porous structures and graphene electroconductivity. This result may be directly related to the three-phase boundary [27–29] where ORR occurs. Doping rare-earth or other metal ions into the perovskite-type composites can tune their catalytic activity and electronic conductivities. Accordingly,  $\text{LaMnO}_3$ –graphene composites were modified by doping with Ca ions with different contents by the same method, and their electrochemical activities for oxygen reduction were examined.

## 2. Experimental

### 2.1. Catalyst preparation

In this paper, thin layer graphene materials were synthesized from natural graphite (Qingdao Graphite Company) using a modified Hummer preparation [30].  $\text{La}_{1-x}\text{Ca}_x\text{MnO}_3$ –graphene composites were prepared by a sol–gel method. In the first step, graphene powders (the mass ratio of graphene to perovskite varied from 0 to 20%) was dispersed to 100 mL distilled water to form suspension, then the suspension solution was subjected to ultrasonic vibration for 1 h. The second, 0.002 mol  $\text{La}(\text{NO}_3)_3$  and  $\text{Ca}(\text{NO}_3)_2$  (the molar ratio of Ca to La varied from 0 to 0.5) were mixed with 0.002 mol  $\text{Mn}(\text{NO}_3)_2$ , which were subsequently dissolved into the suspension. To establish the stoichiometric ratio for the solution, citric acid was successively added (at a molar ratio of 2:1 with respect to the cations) and complexed with metal ion in nitrate to form the stable complex sol. The surface active agent OP-10 was added at a mass ratio of 3:20 with respect to the three nitrates to reduce the capillary force during gel drying process and prevent gel from cracking. The mixed solution was adjusted to pH 9 using aqueous ammonia. The mixture was heated at 60 °C to initiate the polymerization reaction and evaporate excess water until forming the gel. In the end, the gel was initially calcined at 350 °C for 3 h in air and then at 600 °C for 2 h in vacuum to produce final samples. For comparison, the pure  $\text{LaMnO}_3$  powders were prepared under the same condition.

### 2.2. Characterization

The phase identification of perovskite–graphene composites was characterized by X-ray diffraction (XRD,  $D/\text{max} - 2500/\text{pc}$ ) with Cu K $\alpha$  radiation,  $\lambda = 0.15405$  nm. Furthermore, in order to examine the thermal decomposition behavior of the gel, thermogravimetric and differential thermal analysis (DSC/TG, 449C, NETZSCH, SELB, Germany) were carried out at a heating rate of 5 °C  $\text{min}^{-1}$  from 20 to 800 °C in air. The morphology of the composites was investigated by field-emission scanning electron microscopy (FE-SEM, Hitachi S-4800) and transmission electron microscopy (TEM, JEOL-2010) with an accelerating voltage of 200 kV. The binding energy of the elements was measured at about 20 °C by X-ray photoelectron spectroscopy (XPS, ESCALAB250) with a monochromatized Al–Mg X-ray source (Al  $h\nu = 1486.6$  eV; Mg  $h\nu = 1253.6$  eV).

### 2.3. Preparation of air electrodes

Cathode was made by mixing PTFE dispersion (1%) with ethanol to produce a homogeneous paste and then adding acetylene black and catalyst (such as pure  $\text{LaMnO}_3$ , pristine graphene or the prepared composites) to the mixture. The ratio of PTFE:acetylene black: catalyst was controlled (10 wt. %:40 wt. %:50 wt. %). The mixed slurry was coated onto the nickel foam substrate (1 cm  $\times$  1 cm) with a spatula. Subsequently, the former cathode was maintained at a temperature of 60 °C for 24 h to remove residual moisture. The mass of each electrode was about 12.6 mg, which was calculated based on the mass of acetylene black and composites in the cathode electrodes. To prevent the electrolyte leaking out from the cell inside, a proofed breathable film (Shanghai Linflon Film Technology Co., Ltd.) was attached to one side of the air cathode by using 4 Mpa forming pressure under about 20 °C for 30 s. This gas-diffusion electrode supplies air flow channels and reaction sites in the cathode of zinc–air batteries.

### 2.4. Electrochemical measurement

The full battery characterization of the air electrodes was also performed using a home-made Zn–air battery. The cell consisted of an anodic zinc sheet and an air–cathode with 6 M KOH as the electrolyte. The distance between the two electrodes was around 2 cm without any separator and the size of the air–entrance window of the air–electrode was 1  $\times$  1  $\text{cm}^2$ . The galvanostatic discharge measurement was conducted on a Neware Battery test instrument (CT-3008W-5V5Ma-S4; ShenZhen Neware Instrument Company) at about 20 °C, the end voltage of discharge is 1.0 V.

Electrochemical measurements were performed using a three-electrode system in 1 M KOH electrolyte solution: the prepared cathode as a working electrode, a platinum foil (1 cm  $\times$  1 cm), and an Hg/HgO electrode as counter and reference electrodes. Linear sweep voltammetry was conducted on an electrochemical workstation (832C; Shanghai CH Instrument Company) at about 20 °C, and the sweep rate was 5  $\text{mV s}^{-1}$  in a potential range from open potential to  $-0.6$  V. Meanwhile, the AC impedance spectra were measured in a frequency range of 1 MHz–0.1 Hz with an ac signal of 10 mV amplitude.

The ORR activity of the sample was studied with a rotating ring-disk electrode (RRDE) technique by using a pine electrochemical system (AFMSRX rotator and AFCBP1 bipotentiostat). In the RRDE working electrode, the GC disk and Pt ring had geometric areas of 0.196 and 0.125  $\text{cm}^2$ , respectively. The measurements were performed in 0.1 M KOH electrolyte, using a platinum wire counter and an Hg/HgO reference electrode in a three-electrode system. Prior to measurement, the 0.1 M KOH solution was bubbled with pure  $\text{O}_2$ .

(99.9%) at a flow rate of 25 sccm over 0.5 h. The catalyst ink was made from a suspension of 10 mg of composites (the ratio of PTFE:acetylene black was 5:4), 20 mL of Nafion solution (5 wt.%), and 5 mL of isopropanol. Then, the ink was sonicated and dispersed for 30 min. A total of 20  $\mu\text{L}$  catalyst ink was dropped to the glassy carbon working electrode (5 mm in diameter), and the final loading of catalyst was  $57 \mu\text{g cm}^{-2}$ . RRDE measurements were performed by cathodically scanning the disk electrode between 0 and  $-0.60 \text{ V}$  at  $5 \text{ mV s}^{-1}$ , and the Pt ring electrode was held at  $0.5 \text{ V}$ .

### 3. Results and discussion

#### 3.1. TG-DTA analysis

To understand the decomposition behaviors of  $\text{LaMnO}_3$ -graphene precursor and the calcined  $\text{LaMnO}_3$ -graphene sample, the TG-DSC curves were analyzed, and the results are shown in Fig. 1. In the TG curve of the precursor, the weight loss before  $200^\circ\text{C}$  was attributed to the evaporation of free water, and the rapid weight loss of approximately  $220^\circ\text{C}$  was due to the lost process of crystal water. At  $330^\circ\text{C}$ – $400^\circ\text{C}$ , the sharp descendant curve resulted from the decomposition of citric acid complex and nitrate. Meanwhile, the corresponding DSC curve released an amount of heat. In the DSC curve of the precursor, one smaller exothermic

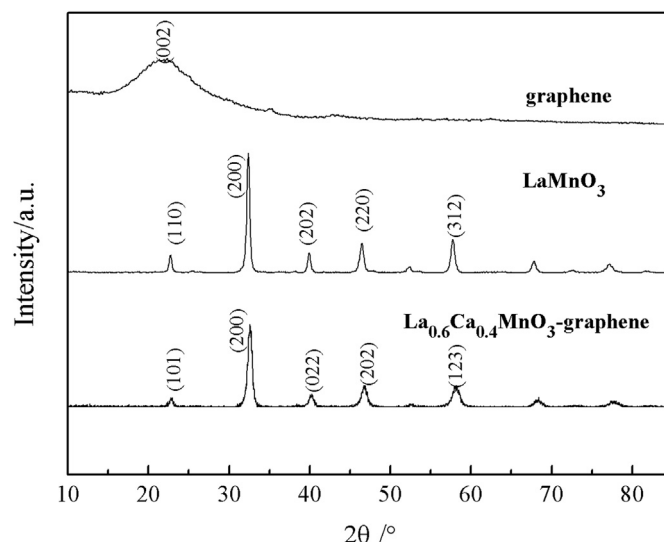


Fig. 2. XRD patterns of graphene,  $\text{LaMnO}_3$  and  $\text{La}_{0.6}\text{Ca}_{0.4}\text{MnO}_3$ -graphene sample (the ratio of graphene to perovskite was 10 wt%).

peak appeared at  $290^\circ\text{C}$ , which corresponded to the decomposition of free citrate combustion.

However, the TG curve of the calcined  $\text{LaMnO}_3$ -graphene sample depicted little weight loss before  $350^\circ\text{C}$ . It only showed a big exothermic peak at  $350^\circ\text{C}$ – $420^\circ\text{C}$ , which was due to the exothermic reactions of graphene and residual amorphous carbon in the air. The DSC curve of the  $\text{LaMnO}_3$ -graphene precursor appeared endothermic peak at about  $600^\circ\text{C}$ , which corresponded to the phase transition. This result indicates that the perovskite crystallized completely at  $600^\circ\text{C}$ . Notably, the weight loss of calcined  $\text{LaMnO}_3$ -graphene sample reached 19%, which was more than the ratio of graphene (10 wt.%). This result is possibly attributed to the amorphous carbon remained in the calcined  $\text{LaMnO}_3$ -graphene sample after massive citric acid was burned.

#### 3.2. XRD analysis

The X-ray diffraction (XRD) patterns of the graphene, pure  $\text{LaMnO}_3$  and  $\text{La}_{0.6}\text{Ca}_{0.4}\text{MnO}_3$ -graphene composite are showed in Fig. 2. Compared with graphite, graphene sheet has a low-intensity diffraction peak for C (002), indicating the short-range order of graphene sheets [31]. The diffraction data of  $\text{LaMnO}_3$  can be indexed to perovskite-type structure, without any miscellaneous peak, which agrees well with the reported data (PDF35-1353). Due to the low content of graphene in the composite, the main diffraction peaks of  $\text{LaMnO}_3$ -graphene composite are similar to that of  $\text{LaMnO}_3$ , which indicates that the presence of graphene dose not change the perovskite-type structure. Comparing with  $\text{LaMnO}_3$ ,  $\text{La}_{0.6}\text{Ca}_{0.4}\text{MnO}_3$  is also the perovskite-type structure. There are also no additional peaks matching the phases of  $\text{La}_2\text{O}_3$  or  $\text{CaO}$  in the diffraction peaks of Ca doped, which agrees well with the reported data (PDF46-0513). The main peaks ( $2\theta = 23.1^\circ, 32.3^\circ, 40.2^\circ, 46.5^\circ$  and  $58.1^\circ$ ) of  $\text{La}_{0.6}\text{Ca}_{0.4}\text{MnO}_3$ -graphene correspond to the perovskite phase (101), (200), (022), (202) and (123) crystal plane, respectively. The above analysis shows that the composite has two-phase structure and perovskite as the main crystalline phase. With graphene as carrier, the perovskite particles showed nucleation and growth. The perovskite' crystallite size was calculated using the Scherrer formula. The lattice parameters are listed in Table 1.

Generally, the  $\text{BO}_6$  octahedron would be distortion to form orthorhombic structure due to the existence of A ion. The tolerance factor ( $t$ ) was defined in the following formula [32].

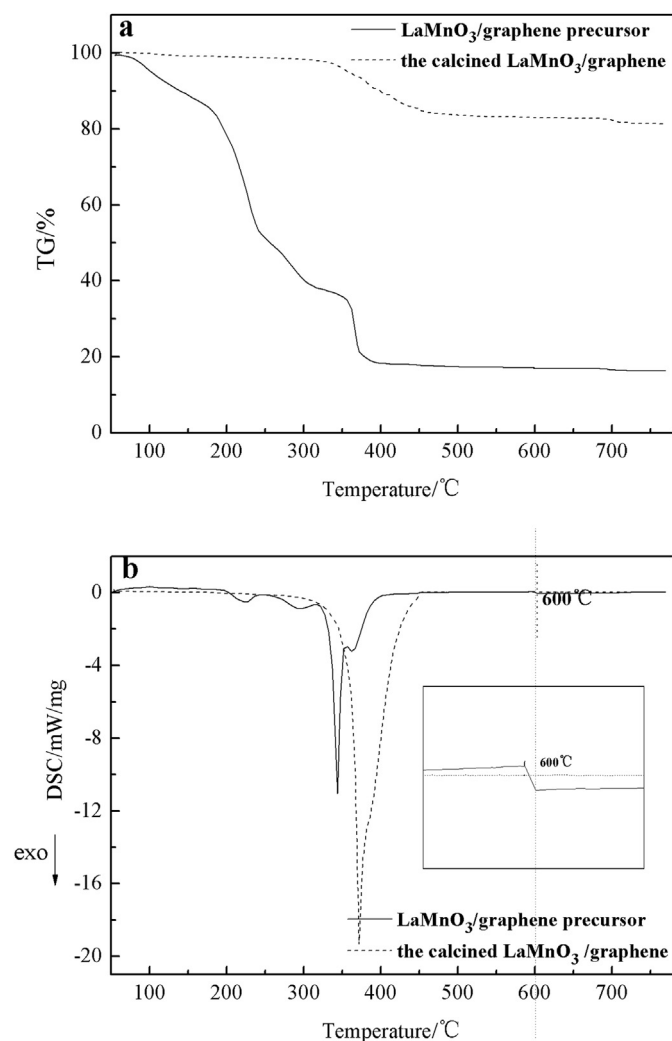


Fig. 1. (a) TG and (b) DSC curves of  $\text{LaMnO}_3$ -graphene precursor and the calcined  $\text{LaMnO}_3$ -graphene sample (the ratio of graphene to perovskite was 10 wt%).

$$(r_A + r_O) = t\sqrt{2}(r_B + r_O) \quad (1)$$

When  $t$  value is 0.75–1.0, the perovskite structure can be remained. When the  $t$  is close to 1, perovskite is the ideal cubic structure. When La ions are partially substituted by Ca, the balance between atoms is destroyed due to the defect was introduced, which make  $t$  value more deviate 1, therefore, the crystal structure had been distortion. The lattice distortion ratio was defined in the following formula [33].

$$\beta^2 \cos^2 \theta = \left(4/\pi^2\right) (\lambda/D_{hkl})^2 + 32(\epsilon^2) \sin^2 \theta \quad (2)$$

where  $D_{hkl}$  is the average grain size,  $\epsilon$  is the lattice distortion ratio,  $\beta$  is the FWHM of  $(hkl)$  peak,  $\theta$  is diffraction angle. According to the formula, the lattice distortions ratio of  $\text{La}_{0.6}\text{Ca}_{0.4}\text{MnO}_3$ -graphene at (101), (200) and (022) crystal planes was  $5.434 \times 10^{-3}$ ,  $4.685 \times 10^{-3}$  and  $3.668 \times 10^{-3}$ , respectively.

### 3.3. FE-SEM analysis

FE-SEM analyses were carried out to observe the morphology of the as-synthesized material (Fig. 3). As shown in Fig. 3a, the as-prepared graphene have a gauze-shaped wrinkles and folds structure, which may be caused by oxygenic functional group and the resultant defects during the preparation of graphene oxide. According to our previous study [26], the as-prepared graphene is about 3  $\mu\text{m}$  in lateral sizes and an average thickness of 1.5 nm. Its surface has some oxygenous groups such as carboxyl and carbonyl group. A typical FE-SEM image of  $\text{La}_{0.6}\text{Ca}_{0.4}\text{MnO}_3$ -graphene composite exhibited a porous structure (Fig. 3b and c). As catalyst of air electrode, its porous structure could greatly increase the three-phase region, thereby improving the mass transfer process.

It can be seen from Fig. 3c that the as-prepared graphene was decorated with dense perovskite nanoparticles, which decreased the agglomeration of nanoparticles. Fig. 3d shows that the perovskite nanoparticles are granular exhibiting a highly crystalline and the size of particles is 15–20 nm. The EDS spectrum of  $\text{La}_{0.6}\text{Ca}_{0.4}\text{MnO}_3$ -graphene composite shown in Fig. 3e indicated the presence of C, O, Mn, Ca, and La elements. The molar ratio of Ca to La was about 3.85:5.95, which indicated that the amount of doping Ca was substantially identical to the theoretical value. The C signal was much weaker than the intensity of La, Mn, and Ca signals, which may be attributed to the low content of graphene. The O content was higher than the theoretical value because of the residual oxygenic functional groups in graphene. The  $\text{La}_{0.6}\text{Ca}_{0.4}\text{MnO}_3$  with interplanar distances of approximately 0.389 nm shown in Fig. 3f corresponded to the (101) plane, which was consistent with the result calculated from the XRD analysis.

### 3.4. XPS analysis

The XPS spectrum of  $\text{La}_{0.6}\text{Ca}_{0.4}\text{MnO}_3$ -graphene composite is shown in Fig. 4. The peak contained all the elements of

$\text{La}_{0.6}\text{Ca}_{0.4}\text{MnO}_3$  (Fig. 4a). Fig. 4b displays the O 1s spectra of  $\text{La}_{0.6}\text{Ca}_{0.4}\text{MnO}_3$ -graphene and  $\text{LaMnO}_3$ -graphene composite. The O 1s spectra were divided into two peaks at 527.6 eV (designated as  $O_L$ ) and 529.7 eV (designated as  $O_C$ ), which were attributed to the contribution of the crystal lattice oxygen ( $\beta$  oxygen) and the chemisorbed oxygen ( $\alpha$  oxygen) [34], respectively. The  $\alpha$  oxygen was an adsorbed oxygen, which can easily lead to ORR, and closely tied up with oxygen vacancies (Vo). The oxygen vacancies (Vo) increased with Ca doping, so the concentration of  $\alpha$  oxygen also increased with Ca doping. Fig. 4b shows that the  $\alpha$  oxygen peak area of  $\text{La}_{0.6}\text{Ca}_{0.4}\text{MnO}_3$ -graphene was apparently higher than that of  $\text{LaMnO}_3$ -graphene, thus, Ca doping was conducive to catalytic performance. In Fig. 4c, the high-resolution curve of Ca 2p region displayed two strong peaks centered at about 345 and 348.5 eV, which were attributed to binding energy of Ca 2p<sub>3/2</sub> and 2p<sub>1/2</sub>, respectively. The spin energy was 3.5 eV, which indicated that the Ca species mainly existed in their +2 valence state. Fig. 4d shows the Mn 2p spectra, the two peaks were located at 642 and 653 eV, which belonged to Mn 2p<sub>3/2</sub> and Mn 2p<sub>1/2</sub>, respectively. The range of Mn 2p<sub>3/2</sub> could be divided into two peaks by fitting. The peaks at 642.3 and 641 eV were assigned to  $\text{Mn}^{4+}$  and  $\text{Mn}^{3+}$ , respectively.

### 3.5. Electrocatalytic activity

Fig. 5a shows the typical discharge curves of air electrodes for  $\text{LaMnO}_3$ -graphene composites in a single cell test for 48 h. The discharge performance was measured in the 6 M KOH electrolyte at a current density of 18  $\text{mA cm}^{-2}$  (1.41  $\text{A g}^{-1}$ ). All discharge curves initially presented upturn and then reached a steady state because of the short period of immersion in the electrolyte, leading to insufficient contact of active material with electrolyte. The discharge curve of the  $\text{LaMnO}_3$  electrode was poorer than those of the  $\text{LaMnO}_3$ -graphene electrodes at the same current density, especially after 25 h. This result demonstrated that  $\text{LaMnO}_3$ -graphene composites had higher stability than that of  $\text{LaMnO}_3$ . It can be seen from the discharge time and voltage plateau level of graphene electrode, the prepared graphene had lower electrical properties because its surface has some structure defect, for instance, -OH groups [35]. Nevertheless, when the surfaces of graphene were modified by  $\text{LaMnO}_3$  particles, the electrochemical properties of the composites were significantly improved, which may be attributed to their synergistic effect. Graphene is not only as supports for  $\text{LaMnO}_3$  particles, but also as electronic conductive channels. The porous structure of composites increased the three-phase interface area, where air electrode ORR occurred. When the ratio of graphene was 10 wt%, the voltage plateau was superior and exhibited the highest performance, which agreed with Fig. 5b.

Fig. 5b shows that the air electrode with  $\text{LaMnO}_3$ /graphene 10 wt% achieved higher reduction current density of 55 and 32  $\text{mA cm}^{-2}$  at -0.60 and -0.50 V, respectively. By contrast, pure  $\text{LaMnO}_3$  delivered 22 and 16  $\text{mA cm}^{-2}$  at an identical potential. These results indicated that the catalytic activity was significant improvement when  $\text{LaMnO}_3$  was compounded with graphene. Nevertheless, excessive content of graphene reduced the catalytic activity, such as  $\text{LaMnO}_3$ /graphene 15 wt% and  $\text{LaMnO}_3$ /graphene 20 wt%. The reduction of activity was due to  $\text{LaMnO}_3$  particles, which were wrapped by large quantities of graphene, thus affecting the catalytic activity of  $\text{LaMnO}_3$  to a certain extent.

The discharge performances of air electrodes for  $\text{La}_{1-x}\text{Ca}_x\text{MnO}_3$ -graphene composites are shown in Fig. 6a (the ratio of graphene was 10 wt. %). The catalytic activity varied with the molar ratio of La to Ca. When  $x$  was from 0.1 to 0.4, both the current density and voltage plateau level (operating voltage) notably increased by increasing the Ca content. The ORR activity was increased because of the following reasons. According to the XPS

**Table 1**  
The lattice parameters of  $\text{LaMnO}_3$  and  $\text{La}_{0.6}\text{Ca}_{0.4}\text{MnO}_3$ -graphene.

Composition	$\text{LaMnO}_3$		$\text{La}_{0.6}\text{Ca}_{0.4}\text{MnO}_3$ -graphene	
PDF (no.)	35-1353		46-0513	
Crystal structure	Orthorhombic		Orthorhombic	
Space group (no.)	Pbnm(62)		Pnma(62)	
$a$ (Å)	5.537		5.443	
$b$ (Å)	5.741		7.683	
$c$ (Å)	7.694		5.454	
Average grain size/(nm)	$D_{110}/(\text{nm})$	22.6	$D_{101}/(\text{nm})$	16.1
	$D_{200}/(\text{nm})$	22.4	$D_{200}/(\text{nm})$	13.3
	$D_{022}/(\text{nm})$	20.9	$D_{022}/(\text{nm})$	13.4



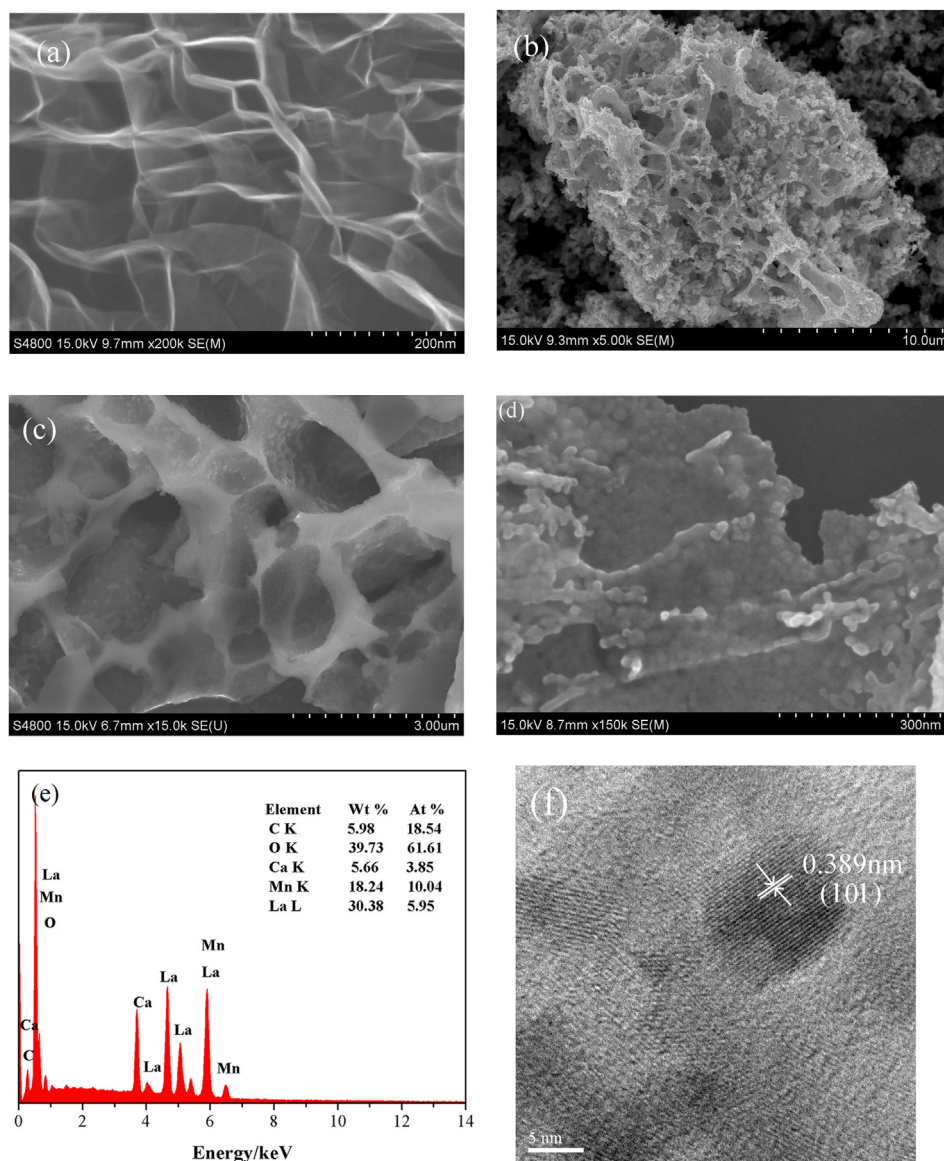


Fig. 3. FESEM images of (a) graphene; (b, c, d) FE-SEM, (e) EDS, (f) HRTEM of  $\text{La}_{0.6}\text{Ca}_{0.4}\text{MnO}_3$ -graphene composite.

result, the concentration of  $\alpha$  oxygen was increased significantly by Ca doping compared with  $\text{LaMnO}_3$ . The  $\alpha$  oxygen was closely tied up with oxygen vacancies ( $\text{V}_\text{O}$ ) [36]. Thus, the oxygen vacancies ( $\text{V}_\text{O}$ ) of  $\text{La}_{1-x}\text{Ca}_x\text{MnO}_3$  increased significantly, which correspondingly enhanced the catalytic reduction activity. In order to maintain the electrically neutral of system, Ca doping make part of  $\text{Mn}^{3+}$  at the B site transform into  $\text{Mn}^{4+}$ , following this reaction:  $\text{LaMnO}_3 + \text{Ca}^{2+} \rightarrow \text{La}^{3+}_{1-x}\text{Ca}^{2+}_x\text{Mn}^{3+}_{1-x}\text{Mn}^{4+}_x\text{O}_3 + \text{La}^{3+}_x$ . The coexistence of  $\text{Mn}^{3+}$  and  $\text{Mn}^{4+}$  led to good electrical conductivity of  $\text{La}_{1-x}\text{Ca}_x\text{MnO}_3$  and provided a good environment for ORR. Meanwhile, the active site of catalytic reduction reaction increased due to the surface enrichment of  $\text{Mn}^{4+}/\text{Mn}^{3+}$  in the oxides, which not only promoted the reduction of oxygen but also reduced polarization [37]. Thus, the performance of electrode is improved. When Ca doping amount reached up to 0.5, the randomization degree of crystal oxygen vacancy distribution was reduced, that is, oxygen vacancy arranged orderly [38], which contributed to electroactivity reduction. Fig. 6b also validated this result, the air electrodes with  $\text{La}_{0.6}\text{Ca}_{0.4}\text{MnO}_3$ -graphene composite showed the highest oxygen

reduction current than that with other components. The current density of air electrode with  $\text{La}_{0.6}\text{Ca}_{0.4}\text{MnO}_3$ -graphene was  $65 \text{ mA cm}^{-2}$  at  $-0.50 \text{ V}$ , which was two times of that with  $\text{LaMnO}_3$ -graphene.

To obtain additional supporting evidence, the EIS characteristic of the air electrode was investigated. Fig. 7 shows that all the impedance plots were composed of a semicircle in the high frequency range and a straight line in the low frequency range because of charge transfer and diffusion processes of oxygen at the electrode/electrolyte interface [39], respectively. The measured impedance spectra were analyzed based on the equivalent circuit, which is shown in the inset.  $L$  is the equivalent inductance,  $C_1$  is the limit capacitance, and  $R_1$  is the ohmic resistance between the reference electrode and the electrode current collector. A major difference is the semicircle in the high frequency range, which corresponded to the charge transfer resistance  $R_2$  caused by the Faradaic reactions and the double-layer capacitance  $C_2$  on the grain surface. The slope of the  $45^\circ$  portion of the curve is called the Warburg resistance  $W$  and  $R_3$ , which is the result of the frequency

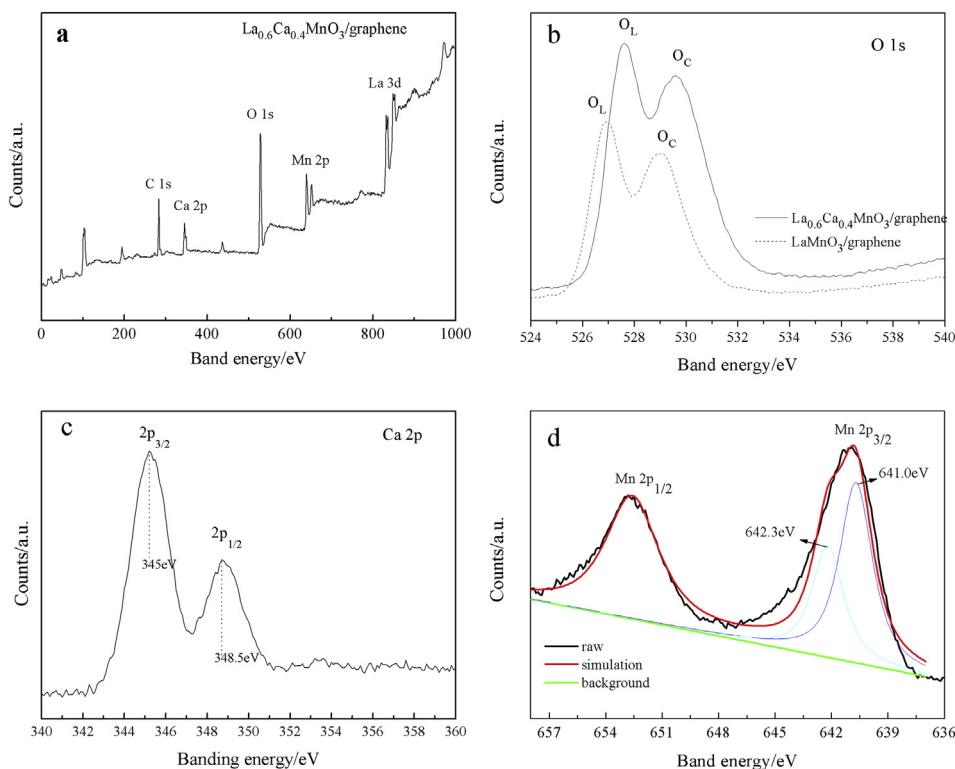


Fig. 4. XPS spectrum of  $\text{La}_{0.6}\text{Ca}_{0.4}\text{MnO}_3$ -graphene composite (a) Overall spectrum, High-resolution curves of (b) O 1s region, (c) Ca 2p region and (d) Mn 2p region.

dependence of ion diffusion/transport in the electrolyte to the electrode surface. The corresponding fitting parameters are listed in Table 2. The calculated charge-transfer resistance for the electrode was decreased from  $3.106 \Omega$  to  $0.9447 \Omega$ , which was probably due to the electroconductivity of graphene. Graphene functioned as an electron acceptor and transmitter in the composites, thus achieving a rapid transport of charge carriers. It can overcome the serious electrochemical polarization in ORR process. Moreover, the increased Warburg resistance was attributed to the increased diffusion and migration pathways of electrolyte ions because of the porous structure of composites.

ORR is a complex electrochemical process, which includes several electrons, hydroxyl transfer steps, and possible intermediates. To understand the mechanism of ORR reaction, these processes must be extended. Scheme 1 describes the potential reaction pathways by which  $\text{O}_2$  reacts at the catalyst surface [12]. The reaction scheme shows that the ORR can occur through the  $k_1$  pathway, where oxygen is electrochemically reduced to  $\text{OH}^-$  by a four-electron process. ORR can also occur via a successive process, where oxygen is initially reduced to hydroperoxide ions  $\text{HO}_2^{\cdot\text{ad}}$  ( $k_2$ ). Subsequently, the  $\text{HO}_2^{\cdot\text{ad}}$  produced in the step  $k_2$  can be further reduced through reaction  $k_3$  to complete the  $2 + 2$  electron transfer, forming the final product of  $\text{OH}^-$ . Meanwhile, some  $\text{HO}_2^{\cdot\text{ad}}$  can be desorbed into the solution ( $k_5$ ) or decomposed into  $\text{OH}^-$  and  $\text{O}_2$  ( $k_4$ ). Because peroxide intermediates can be chemically aggressive toward the catalyst itself, leading to possible degradation of the cell, the preferred reaction product in the cell applications is the four-electron transfer process. Therefore, elucidating the final products for ORR is important in developing a new class of catalysts.

We used RRDE measurements to verify the ORR catalytic pathways of the composites (Fig. 8). The RRDE experiment involves holding the disk at potential  $E_d$ , where the reaction  $\text{O} + ne \rightarrow \text{R}$  produces a cathodic current  $i_d$ . The ring is maintained at a sufficient positive potential  $E_r$ , any R reaching the ring is rapidly oxidized so

that the concentration of R at the ring surface is essentially zero [40]. According to RRDE theory, the overall electron transfer numbers in the ORR process can be calculated using the following equations:

$$n = \frac{4Ni_d}{Ni_d + i_r} \quad (3)$$

where  $n$  is the reaction electron number,  $i_d$  is the disk current,  $i_r$  is the ring current, and  $N$  is the capture coefficient (the value of collection efficiency was found to be 0.22, which is determined using a potassium ferricyanide solution purged with argon). According to the equations, the electron transfer numbers on graphene,  $\text{LaMnO}_3$ ,  $\text{LaMnO}_3$ -graphene and  $\text{La}_{0.6}\text{Ca}_{0.4}\text{MnO}_3$ -graphene electrodes were 1.82, 2.95, 3.42, and 3.60, respectively. Compared with  $\text{LaMnO}_3$ , the number of electron transfer for  $\text{LaMnO}_3$ -graphene composites is larger than  $\text{LaMnO}_3$  because of three reasons. (1) The  $\text{LaMnO}_3$  particles are highly dispersed on the graphene surface, accordingly decrease the agglomeration of nanoparticles, which improving the utilization of  $\text{LaMnO}_3$  and increase the active sites in ORR. (2) As supports for  $\text{LaMnO}_3$  particles, graphene is also electronic conductive channels. This suggested a much smaller charge transfer resistance for the composites during ORR, due to the intimate nanocrystal graphene coupling that enhanced electron transport between  $\text{LaMnO}_3$  and graphene [41]. (3) The porous structure of composites (it can be seen from Fig. 3(b–c)) increased the three-phase interface area, where air electrode ORR occurred [42], therefore, improved the mass transfer velocity for oxygen gas.

Partial substitution of  $\text{La}^{3+}$  by  $\text{Ca}^{2+}$  in  $\text{LaMnO}_3$ -graphene resulted in significant changes on its catalytic activity. Replacement of  $\text{La}^{3+}$  by  $\text{Ca}^{2+}$  induced a positive charge deficiency that was compensated by the oxidation of some  $\text{Mn}^{3+}$  to  $\text{Mn}^{4+}$  and the generation of oxygen vacancies, which greatly promoted the

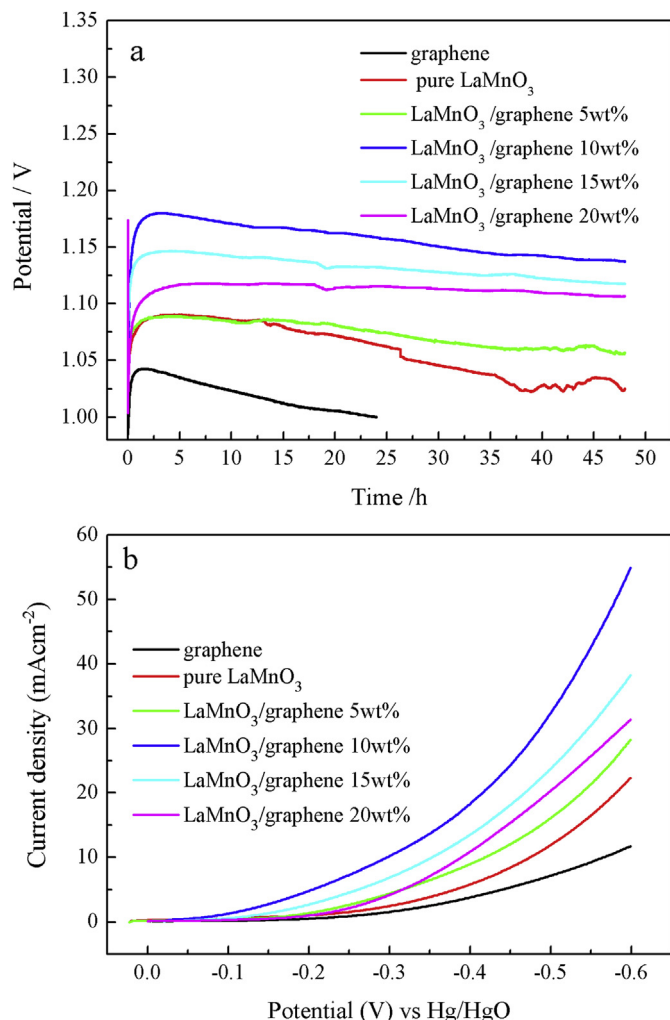


Fig. 5. (a) Discharge curves, (b) polarization curves of air electrodes for different sample.

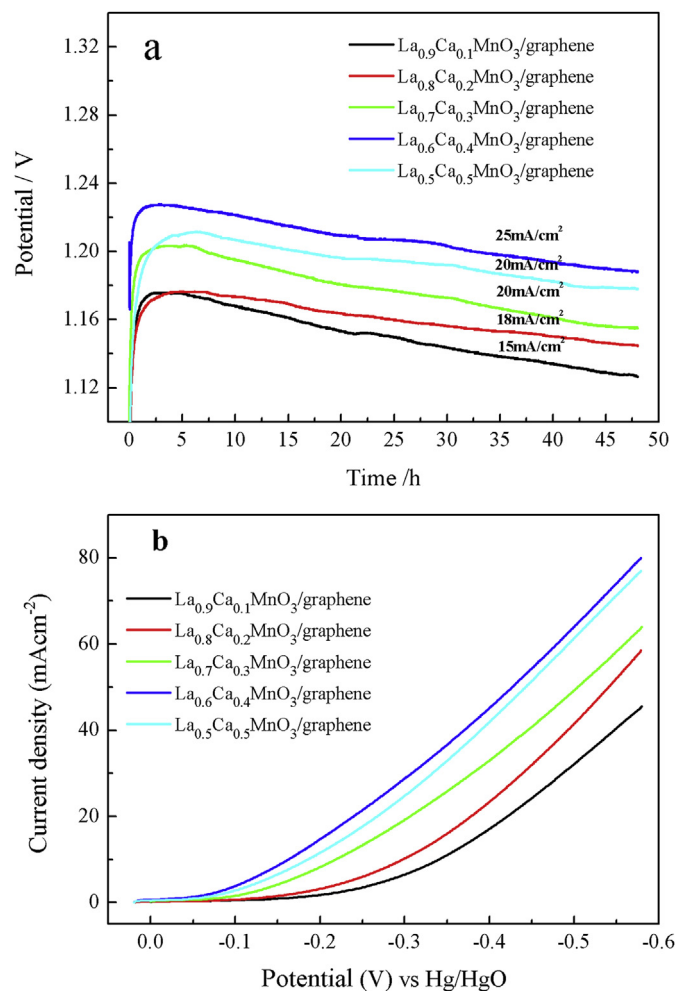


Fig. 6. (a) Discharge curves, (b) polarization curves of air electrodes for  $\text{La}_{1-x}\text{Ca}_x\text{MnO}_3$ -graphene (x = 0.1–0.5) (the ratio of graphene was 10 wt%).

reducibility of the perovskite [43]. With the increasing of Ca doping, the defects concentration in the oxygen lattice is increased, and formed more  $\text{O}^{2-}$  ionic conductor, thus the ORR activity of perovskite is also increased. When Ca doping amount is greater than 0.4, excessive oxygen defects in the crystal structure can absorb free state oxygen, which make the crystal structure changed and restrain the decomposition of  $\text{HO}_2^-$ . Therefore, Ca = 0.4 showed the highest oxygen reduction activity [44]. The RRDE measurement results indicated that  $\text{OH}^-$  (four electrons transferred) and  $\text{HO}_2^-$  (two electrons transferred) coexisted in the three perovskite samples.  $\text{La}_{1-x}\text{Ca}_x\text{MnO}_3$ -graphene did not display a complete four-electron process, but it could also be used as a potential catalyst for a Zn-air cells.

#### 4. Conclusions

$\text{La}_{1-x}\text{Ca}_x\text{MnO}_3$ -graphene composites were successfully synthesized by a sol-gel method as a catalyst for Zn-air cell cathodes, and their electrocatalytic properties were investigated. The results indicated that perovskite phase adhered on the surface of graphene sheets, and adding graphene significantly improved the electrochemical performance of  $\text{LaMnO}_3$ . The Voltage plateau was superior when the ratio of graphene was 10 wt%. Ca doping not only maintained the perovskite structure, but also significantly

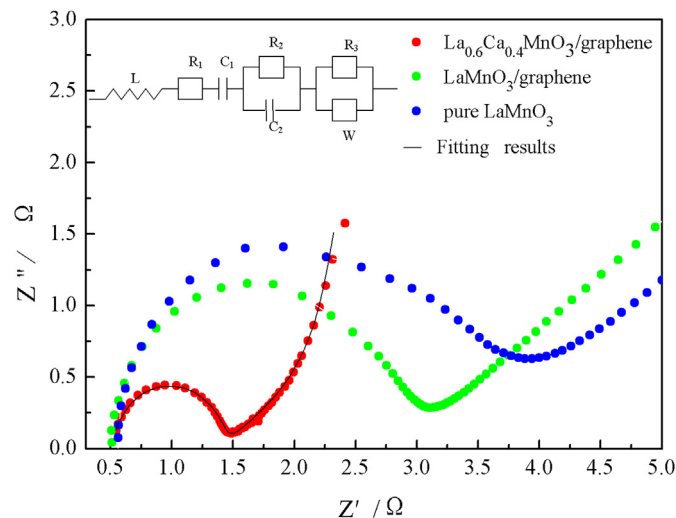
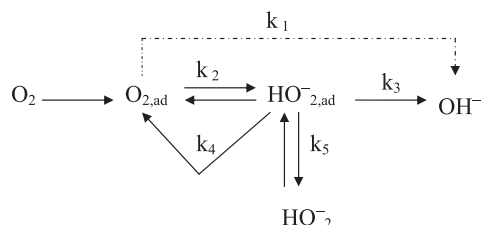
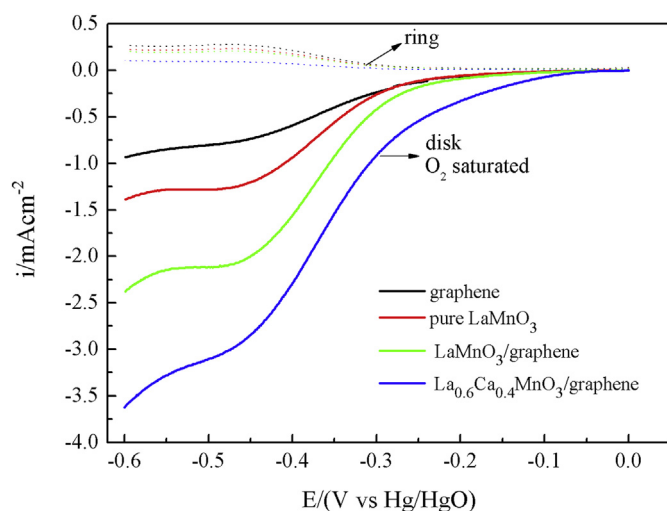


Fig. 7. Nyquist plots of electrodes with  $\text{LaMnO}_3$ ,  $\text{LaMnO}_3$ -graphene and  $\text{La}_{0.6}\text{Ca}_{0.4}\text{MnO}_3$ -graphene, inset is the electrical equivalent circuit used for fitting impedance spectra.

**Table 2**

The corresponding fitting parameters of the experimental impedance spectra based upon the proposed equivalent circuit in Fig. 7.

Sample	$R_1$	$C_1$	$R_2$	$C_2$	$R_3$	$W$
Pure LaMnO <sub>3</sub>	0.8082	0.03404	3.106	7.24E-7	39.47	0.01346
LaMnO <sub>3</sub> /graphene	0.7714	0.05074	2.47	8.398E-7	14.14	0.03563
La <sub>0.6</sub> Ca <sub>0.4</sub> MnO <sub>3</sub> /graphene	0.4871	0.09105	0.9447	7.73E-6	1.463	0.1573

**Scheme 1.** Reaction scheme for the oxygen reduction reaction in alkaline medium.

**Fig. 8.** Disk current density and ring current density collected on LaMnO<sub>3</sub>, graphene, LaMnO<sub>3</sub>–graphene and La<sub>0.6</sub>Ca<sub>0.4</sub>MnO<sub>3</sub>–graphene electrodes during the ORR at rotation rate of 1600 rpm (all in oxygen saturated 0.1 M KOH electrolyte at 5 mV s<sup>−1</sup> scan rate). Disk current ( $i_d$ ) (solid line) is shown on the lower half and ring current ( $i_r$ ) (dotted line) is shown on the upper half of the graph.

improved the electrocatalytic activity for the ORR, and La<sub>0.6</sub>Ca<sub>0.4</sub>MnO<sub>3</sub>–graphene exhibited the best catalytic activity. The electron transfer number of La<sub>0.6</sub>Ca<sub>0.4</sub>MnO<sub>3</sub>–graphene was 3.6, which was calculated from the RRDE measurement result. This finding indicated that the sample exhibited considerable catalytic activity for the ORR. Therefore, this study shows the possibility to adjust LaMnO<sub>3</sub> ORR activity through a simple process. This correlation may also extend to other perovskite systems.

## Acknowledgments

The authors gratefully acknowledge the support of the Research Program of the College Science & Technology of Hebei Province (No.

QN20131026), the Technology Support Program of Hebei Province (No. 13214903).

## References

- [1] A. Puapattanakul, S. Therdthianwongb, A. Therdthianwongc, N. Wongyao, *Energy Proc.* 34 (2013) 173–180.
- [2] P. Sapkota, H. Kim, *J. Ind. Eng. Chem.* 15 (2009) 445–450.
- [3] T.J. Schmidt, V. Stamenkovic, M. Arenz, N.M. Markovic, P.N. Ross, *Electrochim. Acta* 47 (2002) 3765–3776.
- [4] L. Xiong, A. Manthiram, *J. Mater. Chem.* 14 (2004) 1454–1460.
- [5] M. Nesselberger, S. Ashton, J.C. Meier, I. Katsounaros, K.J. Mayrhofer, M. Arenz, *J. Am. Chem. Soc.* 133 (2011) 17428–17433.
- [6] Y.L. Tsai, K.L. Huang, C.C. Yang, J.S. Ye, L.S. Pan, C.L. Lee, *Int. J. Hydrogen Energy* 39 (2014) 5528–5536.
- [7] Y.H. Shih, G.V. Sagar, S.D. Lin, *J. Phys. Chem. C* 2008 (112) (2008) 123–130.
- [8] A.C. Garcia, E.A. Ticianelli, *Electrochim. Acta* 106 (2013) 453–459.
- [9] J. Guo, A. Hsu, D. Chu, R. Chen, *J. Phys. Chem. C* 114 (2010) 4324–4330.
- [10] Z.H. Sheng, H.L. Gao, W.J. Bao, F.B. Wang, X.H. Xia, *J. Mater. Chem.* 22 (2012) 390–395.
- [11] Z.H. Fu, X.J. Lin, T. Huang, *J. Solid State Electrochem.* 16 (2012) 1447–1452.
- [12] E. Fabbri, R. Mohamed, P. Levecque, O. Conrad, R. Kotz, T.J. Schmidt, *Chem-ElectroChem* 2 (2014) 338–342.
- [13] C.A. Hancock, A.L. Ong, P.R. Slater, J.R. Varcoe, *J. Mater. Chem. A* 9 (2014) 3047–3056.
- [14] J. Sunarso, A.A. Torriero, W. Zhou, P.C. Howlett, M. Forsyth, *J. Phys. Chem. C* 116 (2012) 5827–5834.
- [15] M. Yuasa, N. Yamazoe, K. Shimano, *J. Electrochem. Soc.* 158 (2011) A411–A416.
- [16] K. Miyazaki, K.I. Kawakita, T. Abe, T. Fukutsuka, K. Kojima, Z. Ogumia, *J. Mater. Chem.* 21 (2011) 1913–1917.
- [17] V. Neburchilov, H. Wang, J.J. Martin, W. Qu, *J. Power Sources* 195 (2010) 1271–1291.
- [18] R.S. Edwards, K.S. Coleman, *R. Soc. Chem.* 5 (2013) 38–51.
- [19] M.H. Seo, S.M. Choi, H.J. Kim, W.B. Kim, *Electrochem. Commun.* 13 (2011) 182–185.
- [20] L. Qu, Y. Liu, J.B. Baek, L. Dai, *ACS Nano* 4 (2010) 1321–1326.
- [21] E.J. Lim, S.M. Choi, M.H. Seo, Y. Kim, S. Lee, W.B. Kim, *Electrochem. Commun.* 28 (2013) 100–103.
- [22] F.B. Wang, J. Wang, L. Shao, Y. Zhao, X.H. Xia, *Electrochem. Commun.* 38 (2014) 82–85.
- [23] Y. Liang, Y. Li, H. Wang, J. Zhou, J. Wang, T. Regier, H. Dai, *Nat. Mater.* 10 (2011) 780–786.
- [24] Y. Liang, H. Wang, J. Zhou, Y. Li, J. Wang, T. Regier, H. Dai, *J. Am. Chem. Soc.* 134 (2012) 3517–3523.
- [25] Z.S. Wu, S. Yang, Y. Sun, K. Parvez, X. Feng, K. Müllen, *J. Am. Chem. Soc.* 134 (2012) 9082–9085.
- [26] J. Hu, J.H. Ma, L.N. Wang, H. Huang, *J. Alloys Compd.* 583 (2014) 539–545.
- [27] J. Xiao, D.H. Mei, X.L. Li, W. Xu, D.Y. Wang, G.L. Graff, W.D. Bennett, Z. Nie, I.V. Saraf, I.A. Aksay, J. Liu, J.G. Zhang, *Nano Lett.* 11 (2011) 5071–5078.
- [28] J.G. Zhang, D.Y. Wang, W. Xu, J. Xiao, R.E. Williford, *J. Power Sources* 195 (2010) 4332–4337.
- [29] J. Xiao, D.H. Wang, W. Xu, D.Y. Wang, R.E. Williford, J. Liu, J.G. Zhang, *J. Electrochem. Soc.* 157 (2010) 487–492.
- [30] X. Du, P. Guo, H.H. Song, X.H. Chen, *Electrochim. Acta* 5 (2010) 4812–4819.
- [31] J. Yan, T. Wei, B. Shao, F.Q. Ma, Z.J. Fan, M.L. Zhang, C. Zheng, Y.C. Shang, W.Z. Qian, F. Wei, *Carbon* 48 (2010) 1731–1737.
- [32] Y. Teraoka, M.D. Wei, S. Kagawa, *J. Mater. Chem.* 8 (1998) 2323–2325.
- [33] X.T. Dong, G.Y. Hong, D.C. Yu, *J. Inorg. Mater.* 11 (1996) 542–546.
- [34] H. Yang, J.X. Zhang, G.J. Lin, T. Xian, J.L. Jiang, *Adv. Powder Technol.* 24 (2013) 242–245.
- [35] J. Ito, J. Nakamura, A. Natori, *J. Appl. Phys.* 103 (2008) 113712.
- [36] Y. Teraoka, *Solid State Ionics* 48 (1991) 207–212.
- [37] Q.B. Wang, B.S. Dou, Z.L. Yu, *Chin. J. Catal.* 19 (1998) 116–120.
- [38] Z.J. Kang, Y.H. Yao, X. Zheng, *J. Mol. Catal. (China)* 19 (2005) 473–476.
- [39] M. Cheriti, A. Kahoul, *Mater. Res. Bull.* 47 (2012) 135–141.
- [40] C. Jin, X.C. Cao, L.Y. Zhang, C. Zhang, R.Z. Yang, *J. Power Sources* 241 (2013) 225–230.
- [41] L. Genies, Y. Bultel, R. Faure, R. Durand, *Electrochim. Acta* 48 (2003) 3879–3890.
- [42] F. Bidault, D.J.L. Brett, P.H. Middleton, N.P. Brandon, *J. Power Sources* 187 (2009) 39–48.
- [43] H. Feng, J. Du, X.p. Han, F.Y. Cheng, J. Chen, *Chin. J. Inorg. Chem.* 29 (2013) 1617–1625.
- [44] S.D. Song, Z.Y. Tang, L.Z. Pan, J.M. Nan, *Acta Chim. Sin.* 63 (2005) 363–371.